Vacancy-defect Semiconductor Quantum Dots Induced an S-scheme Charge Transfer Pathway in 0D/2D Structures under Visible-Light Irradiation

Feng Bi[1#], Yuetan Su[1#], Yili Zhang[3], Meiling Chen[1], Jawwad A. Darr[4], Xiaole Weng[1, 2] and Zhongbiao Wu[1]*

[1] Key Laboratory of Environment Remediation and Ecological Health, Ministry of Education, College of Environmental and Resource Sciences, Zhejiang University, 866 Yuhangtang Road, Hangzhou 310058, P. R. China.

[2] ZJU-Hangzhou Global Scientific and Technological Innovation Center, 311200 Hangzhou, P. R. China.

[3] Shanghai Municipal Engineering Design Institute Group Co., Ltd, 901 North Zhongshan (2nd) Road, Shanghai 200092, P. R. China.

[4] Christopher Ingold Laboratories, Department of Chemistry, University College London, 20 Gordon Street, London WC1H 0AJ, United Kingdom.

[*]Corresponding author: xlweng@zju.edu.cn

[#]These authors contributed equally to this work.

Abstract: Designing heterojunctions with a feasible charge transfer pathway is a promising strategy for establishing highly efficient artificial photosystems. The step-scheme (S-scheme) heterojunction has shown considerable potential in enhancing redox ability and charge transfer of photocatalysts. Herein, a hierarchical heterojunction involving vacancy-defect TiO_2 quantum dots (QDs) and 2D g-C_3N_4 nanosheets was constructed using a multi-step assembly strategy. Computational and experimental studies show that the vacancy-defect TiO_2 QDs can induce an S-scheme charge transfer pathway in the 0D/2D heterojunction under visible-light irradiation, which greatly improved the redox ability of charge carriers, enhanced the charge transfer and separation at interfaces, and facilitated the H_2O adsorption and dissociation. This results in over 10-fold increase in hydrogen evolution reaction (HER) of photocatalytic water splitting for a wide range of carbon nitrides. The values achieved compare favorably with the best carbon nitride photocatalysts developed to date.

Keywords: S-scheme, quantum dots, defect, TiO_2, photocatalysis

List of abbreviations

·QDs: Quantum dots

·NSs: Nanosheets

·CHFS: Continuous hydrothermal flow system

·sc-H_2O: Supercritical water

·DFT: Density functional theory

·EPR: Electron paramagnetic resonance

·PALS: Positron annihilation lifetime spectroscopy

·PL: Photoluminescence spectroscopy

·TRPL: Time-resolved photoluminescence

·EIS: Electrochemical impedance spectroscopy

·HR-TEM: High resolution transmission electron microscopy

·AFM: Atomic force microscopy

·FFT: Fast Fourier transform

·FT-IR: Fourier-transform infrared spectroscopy

·TiBALD: Titanium(IV) bis(ammonium lactato)dihydroxide

·TEOA: Triethanolamine

·HER: Hydrogen evolution reaction

·V_O: Oxygen vacancy

1. Introduction

Semiconductor quantum dots (QDs) are promising materials for establishing highly efficient artificial photosystems [1, 2]. Comparing to their bulk counterparts, these materials can offer abundant surface uncoordinated sites for photochemical reaction, but exhibit unstable structure, higher recombination of photoinduced electrons and limited light response due to quantum confinement [3, 4]. To overcome these shortcomings, semiconductor QDs are usually loaded on a two-dimensional (2D) host forming the hierarchical 0D/2D heterojunctions with inhibited self-aggregation and enhanced interfacial charge transfer, contributing to greatly increased photocatalytic activities in H_2 production, CO_2 reduction and pollutant degradation [5-7].

Given the aforementioned benefits of 0D/2D heterojunctions, the materials still need to further improve redox ability and enhance charge migration efficiency for establishing highly efficient energy conversion and environmental control [8, 9]. This demands their structures with a spatial distribution of reduction and oxidation potentials, and a matched band alignment in quantum-to-bulk hybrids. Amongst currently developed heterojunctions, an innovative step-scheme (S-scheme) heterojunction has been recently proposed by Yu et al [10, 11]. This heterojunction consists of two n-type semiconductors, with the reduction-type photocatalyst (RP) of more negative conduction band (CB) position and oxidation-type photocatalyst (OP) of more positive valance band (VB) position. Under light irradiation, the photoelectrons and holes can accumulate separately at the lower VB and higher CB positions in the structure [11, 12], which simultaneously ensures the stronger redox ability of photoinduced elecrons and holes [13, 14]. Consequently, by combining the benefits of 0D/2D and S-scheme heterojunctions, we can expect a novel 0D/2D S-scheme composite with excellent light harvesting capability, effective

photogenerated electrons separation and transfer, and enhanced redox ability simultaneously [11, 12].

However, constructing such a 0D/2D S-scheme nanocomposite faces a challenge of how to precisely tune the band offsets acquired in the quantum-to-bulk hybrids. This usually requires the optimization on photochemical properties of semiconductor QDs, aiming to adjust the band alignment to match the 2D host. Difficulties can thus arise in terms of preserving the QD size and controlling their surface coordination environments during the optimization processing, as surface engineering of QDs generally needs harsh conditions [15, 16], which can coarsen the QDs and destroy their surface chemistry. Moreover, despite the significant growth in the development of 0D/2D heterojunctions, the vast majority of QDs used to date are sulfides, vanadates and perovskites (e.g., CdS, Ag_2S, $AgVO_3$ and $CsPbI_3$) [5, 17, 18]. These QDs are either toxic to the environment due to the use of heavy metals or limited to large-scale production owing to their complex synthesis processes [19, 20], leading to the unfeasibility for industrial applications.

Based on the aforementioned issues, this work aims to shed light on three challenges for developing the innovative 0D/2D S-scheme heterojunction: (1) constructing an environmental-friendly 0D/2D heterojunction by using nontoxic semiconductor QDs and 2D host with a matched band alignment; (2) developing a scalable approach for the manufacture and optimization of semiconductor QDs and their OD/2D heterojunctions to meet industrial demands; (3) establishing an innovative 0D/2D S-scheme nanocomposite with the benefits of extended light harvesting (in particular visible-light), effective photogenerated electrons migration, and enhanced redox power simultaneously.

Firstly, we employed a continuous hydrothermal supercritical water (sc-H_2O) flow reactor (**Figure S1**) [21] to manufacture the earth-abundant and environmental-friendly TiO_2 QDs. Such processes have been shown to deliver scalable and reproducible QD particles for a range of oxide materials (e.g., TiO_2, CeO_2, Co_3O_4, ZnO, NiO) [22]. The process is operated under high temperature (approximately 450 °C) and pressure (approximately 24.1 MPa), which can effectively preserve the QD size in the subsequent surface engineering. The obtained TiO_2 QDs bounded with lactate molecules owning to the use of titanium(IV) bis(ammonium lactato)dihydroxide (TiBALD) precursor [23, 24], which was then loaded onto graphitic carbon nitride (g-C_3N_4) nanosheets under sonication (see **Figure 1a**). In the final step, the composites were heat-treated in an inert N_2 atmosphere from 100 to 300 °C, which oxidized the bound lactate molecules and scavenged the labile O from the TiO_2 surface; this introduces abundant vacancy defects on the TiO_2 QDs surface. Subsequent computational and experimental studies confirmed that, the vacancy-defect TiO_2 QDs with a matched band alignment to g-C_3N_4, have induced an S-scheme charge transfer pathway within the heterojunction under visible illumination. This results in an over 10 times increase in photocatalytic hydrogen evolution rate (HER) from water for a great variety of carbon nitrides. The values achieved compare favorably with the best carbon nitride photocatalysts developed to date.

2. Experimental Section

2.1 Fabrication of catalysts

2.1.1. Fabrication of vacancy-defect TiO_2 QDs

Ultrafine TiO_2 QDs were fabricated via a continuous hydrothermal flow system (CHFS, details are provided in supplementary **Section S1**, **Figure S1**), as was reported in our previous

116 work [24]. Defective TiO_2 QDs (denoted as TiO_2-OV) were obtained by further heating the pristine
117 TiO_2 QDs under N_2 at different temperatures (100, 200, 300 °C) for 2 h, which were denoted as
118 TiO_2-X (X represents the temperature).

119 *2.1.2. Fabrication of g-C_3N_4 NSs*

120 g-C_3N_4 nanosheets (NSs) were synthesized by an oxidation etching route using
121 dicyandiamide as precursor [25, 26]. The synthetic method was provided in the supplementary
122 document.

123 *2.1.3. Fabrication of defective TiO_2 QDs/g-C_3N_4 NSs.*

124 TiO_2 QDs/g-C_3N_4 NSs (denoted as TiO_2/g-C_3N_4) were fabricated using a multi-step assembly
125 strategy. Especially, a certain amount (g) of TiO_2 QDs and 0.1 g g-C_3N_4 NSs were added into 40
126 mL distilled water, with the pH at approximately 6 according to their Zeta potential measurements
127 (see **Figure S2**). Subsequently, after ultrasonication for 40 min, the mixture was then centrifuged
128 and washed with ultrapure water and ethanol, which was dried at 80 °C for 12 h to obtain the final
129 products. TiO_2/g-C_3N_4 composites with different mass ratios (2:1, 1:1, 1:2, 1:3, and 1:4) were
130 prepared by adjusting the added amounts of TiO_2. To fabricate defective TiO_2 QDs/g-C_3N_4 NSs
131 (denoted as TiO_2-OV/g-C_3N_4) heterojunction, the TiO_2/g-C_3N_4 (1:2) were further heat-treated at
132 different temperatures (100, 200, 300 °C) for 2 h under N_2 atmosphere (denoted as TiO_2/g-C_3N_4-
133 X, X represents the temperature).

134 ***2.2 Characterization of catalysts***

135 Details of characterization techniques, including X-ray diffraction (XRD), Fourier-transform
136 infrared (FT-IR), transmission electron microscopy (TEM), atomic force microscope (AFM), UV-

Vis diffuse reflection spectra (UV-Vis DRS), electron paramagnetic resonance (EPR), X-ray photoelectron spectroscopy (XPS), Kelvin probe force microscopy (KPFM), steady-state photoluminescence (PL), time-resolved photoluminescence (TRPL), and positron annihilation lifetime spectroscopy (PALS) are described in the supplementary **Section S2–S3**.

2.3 Photocatalytic and photoelectrochemical performance evaluation

Briefly, photocatalytic activities for hydrogen evolution were tested in a quartz reactor. Especially, the catalyst powders (50 mg) were added into 50 mL of 10 vol% triethanolamine (TEOA) aqueous solution. Before irradiation, the suspension was cleansed with Ar for 15 min to remove dissolved O_2 from the system. Then 1.2 wt% Pt as co-catalysts were in-situ photodeposited onto the surface of samples by photoreduction of H_2PtCl_6. Moreover, the testing temperature was maintained at 25 °C. The H_2 production properties were measured by Agilent 7890A gas chromatograph (GC, Agilent, US), with Ar as the carrier gas. The Xe lamp (300 W, 400 nm cut-off filter, PLS-SXE300, Perfectlight, China) was served as the visible light source.

Additional details of photoelectrochemical measurements are available in supplementary **Section S4**.

2.4 Computational methods

Density fucntional theory (DFT) study was performed to investgate structural characteristics, charge density difference, Bader charge, moluecule adsorption and Gibbs free energy using a VASP code [27]. The configuration was geometrically optimized to obtain the most stable adsorption configuration with the lowest energy. To understand the adsorbate on the substrate catalyst, the adsorption energy (E_{ads}) was defined as:

$$E_{\text{ads}} = E_{\text{total}} - E_{\text{adsorbate}} - E_{\text{substrate}} \quad \text{Equation (1)}$$

where E_{total} was total energy of the whole system after adsorption, and $E_{\text{adsorbate}}$ and $E_{\text{substrate}}$ represented the energies of the energies of the adsorbate and catalyst, respectively. A negative value corresponds to an exothermic process. Further details are shown in supplementary **Section S5.**

3. Results and Discussion

3.1. Defective optimization of TiO_2 QDs

To preserve the TiO_2 QD size and uncoordinated surface during the manufacturing process, a continuous sc-H_2O flow synthesis process was employed to prepare TiO_2 QDs from a TiBALD water-soluble precursor; see supplementary data for details of sc-H_2O syntheses and catalyst characterizations. Because the TiO_2 QDs were fabricated under a high temperature and pressure condition (T=450 °C and P_c=24.1 MPa), subsequent heat treatments can not coarsen the QDs. As demonstrated in **Figure S3**, up to 300 °C, nearly identical 3–10 nm TiO_2 QDs were preserved. Powder XRD (**Figure S4**–**S6**) verified that the crystallite sizes of TiO_2 QDs were maintained at approximately 6.2 ± 0.2 nm (as calculated via Rietveld refinement) after the heat-treatments, with the lattice parameters preserved at a=b=3.79(1) Å and c=9.50(1) Å (**Table S1**).

After being subjected to low-temperature EPR and PALS, the relative concentration of oxygen vacancies on the TiO_2 QDs increased with the heat-treatment temperature (100–300 °C). The EPR spectra (**Figure 1b**) contained an oxygen vacancies signal (i.e., g=2.002) in TiO_2 anatase [28], whose intensity increased at higher temperatures. This indicated that more oxygen vacancies were formed owing to the efficient removal of surface lactate species at elevated temperatures. The PALS data (**Figure 1c** and **Table S2**) yielded three lifetime components for the pristine and

heat-treated TiO_2 QDs. The longest component (τ_3, ca. 3.0−4 ns) was attributed to positron annihilation at interfaces [8, 29], which accounted for <1% of the relative intensity. The shortest component (τ_1, ca. 160−200 ps) corresponded to free annihilation of positrons in the defect-free crystal or that in small V_O [8, 29], accounting for approximately 5−13% of the relative intensity. Another component (τ_2, ca. 330−350 ps), accounting for approximately 87%–95% of the relative intensity, originated from Ti^{3+}–V_O associated with a large defect size [30]. In agreement with the EPR analyses, the dominant relative intensity (I_2), which can quantify the abundance of Ti^{3+}–V_O, increased with heat-treatment temperature. These results further confirm that the relative concentration of V_O in the TiO_2 QDs could be readily tuned by adjusting the heat-treatment temperature.

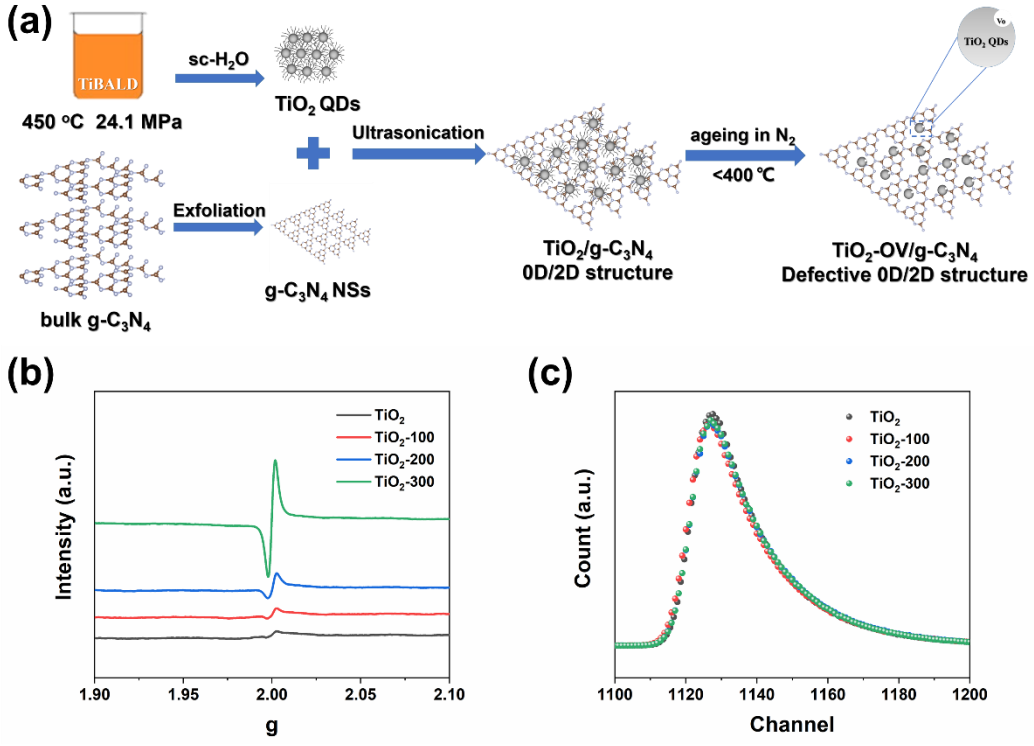

Figure 1. (a) Schematic diagram for preparing the defective 0D/2D TiO_2-OV/g-C_3N_4 using a combined sc-H_2O route. (b) EPR and (c) positron lifetime spectra of TiO_2 QDs that were aged at different temperatures (100, 200 and 300 °C).

3.2 Fabrication of vacancy-defect TiO_2 QDs/g-C_3N_4 heterojunction

To construct vacancy-defect TiO_2 QDs and *g*-C_3N_4 heterojunctions, the obtained TiO_2 from the sc-H_2O process was subsequently loaded onto exfoliated g-C_3N_4 NSs under ultrasonication, followed by heat-treatments in N_2 atmosphere from 100 to 300 °C. The 0D/2D heterojunction was analyzed via TEM (**Figure 2a**) and AFM (**Figure 2b**), yielding an average thickness of 4.0 nm (approximately10 layers of g-C_3N_4 NSs). High-resolution TEM (HRTEM; **Figure 2c–e**) further showed that, in the TiO_2-OV/*g*-C_3N_4 heterojunction, the spherical TiO_2-OV were confined to the g-C_3N_4 NSs with fringe intervals of 0.346 nm, which were assigned to TiO_2 anatase (101) lattice fringe, and the corresponding fast Fourier transform (FFT) pattern (**Figure 2f**) suggested that the anatase particles were single crystals. FT-IR was used to evaluate the chemical structure and interaction of the obtained TiO_2/g-C_3N_4 heterojunction. The spectra for the heterojunction (**Figure S7**) showed characteristic vibrations of both TiO_2 and g-C_3N_4, indicating proximal contact in their junctions. The slight shift of the N–H (3159 cm^{-1}) and Ti–O–Ti (503 cm^{-1}) bands for the composite suggested that the major interfacial interaction was between Ti 3d and N 2p orbitals, consistent with a previous report [31].

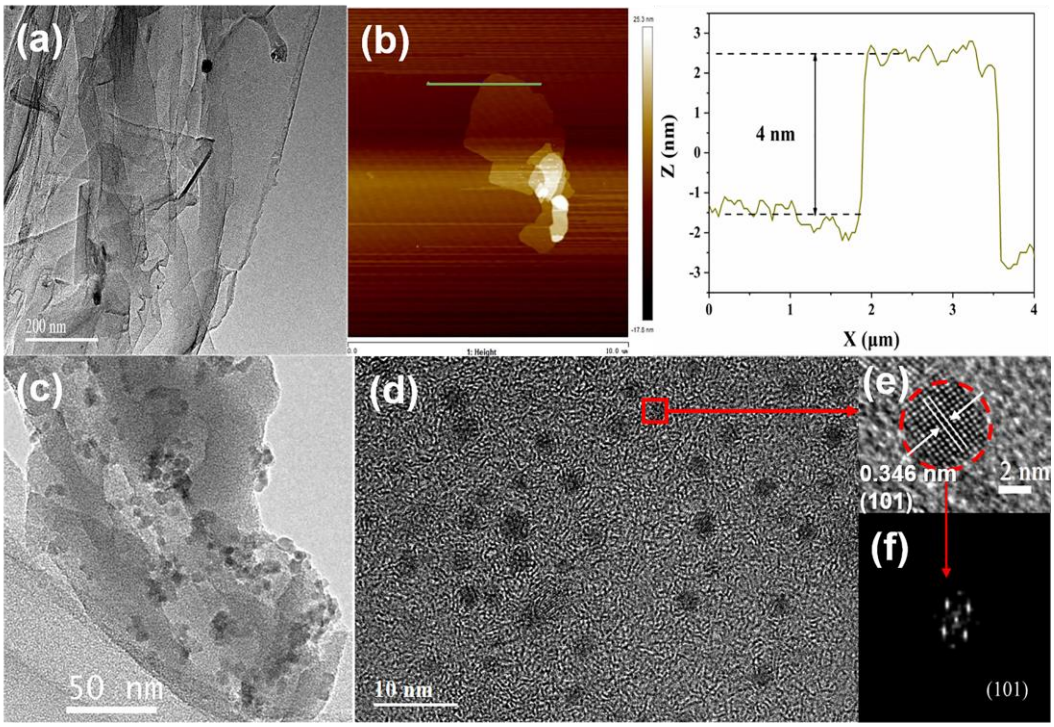

Figure 2. (a) TEM and (b) AFM images of g-C_3N_4 NSs; (c) TEM and (d) HR-TEM image of TiO_2-OV/g-C_3N_4 heterojunction; (e) HR-TEM image and (f) corresponding FFT pattern of a single TiO_2 embedded on g-C_3N_4 and aged at 300 °C.

3.3 Confirmation of the S-scheme charge transfer pathway in 0D/2D heterojunctions

To explore the internal charge transfer pathway amongst TiO_2 QDs, TiO_2-OV, and g-C_3N_4, their optical properties were first examined using UV-Vis DRS (**Figure 3a**). The adsorption edge of TiO_2 QDs was measured at 391 nm with a band gap of 3.17 eV, indicating that this material is inactivation under visible-light illumination. Further ageing of the TiO_2 QDs from 100 to 300 °C exhibited a gradual red-shift in the UV-Vis DRS spectra (**Figure S8**), and in particular, the TiO_2 QDs aged at 300 °C showed an adsorption edge at 418 nm with a corresponding bandgap energy of 2.97 eV, which is activated under visible illumination, and has been used in subsequent photochemical analyses (denoted as TiO_2-OV). In addition, the g-C_3N_4 exhibited a sharp adsorption edge at ca. 454 nm (bandgap, 2.73 eV), similar to a previous report [32].

On the basis of Mott-Schottky (M-S) plots, the flat-band potentials of TiO_2 QDs, TiO_2-OV, and g-C_3N_4 were calculated at −1.037 V, −1.018 V, and −1.109 V (*vs.* Ag/AgCl, pH=7), respectively (**Figure S9**), approximately equal to their Fermi levels in electrolytic solution [33]. The observed positive slope values of the straight part of M-S plots indicate these materials are all n-type semiconductors [34]. To investigate their band structures, valance band X-ray photoelectron spectroscopywere performed (VB-XPS; **Figure 3b**). Typically, for a semiconductor, the VB-XPS spectra correspond to the energy difference between VB position and the Fermi level [35, 36]. Thus, by combining the Fermi levels and VB-XPS measurements (summarized in **Table S3** and shown in **Figure 3c**), the CB and VB positions of TiO_2 QDs were calculated at −0.89 and 2.28 V (*vs.* normal hydrogen electrode (NHE), pH=0), those of TiO_2-OV were at −0.67 and 2.30 V (*vs.* NHE, pH=0), and those of g-C_3N_4 were at −0.93 and 1.80 V (*vs.* NHE, pH=0).

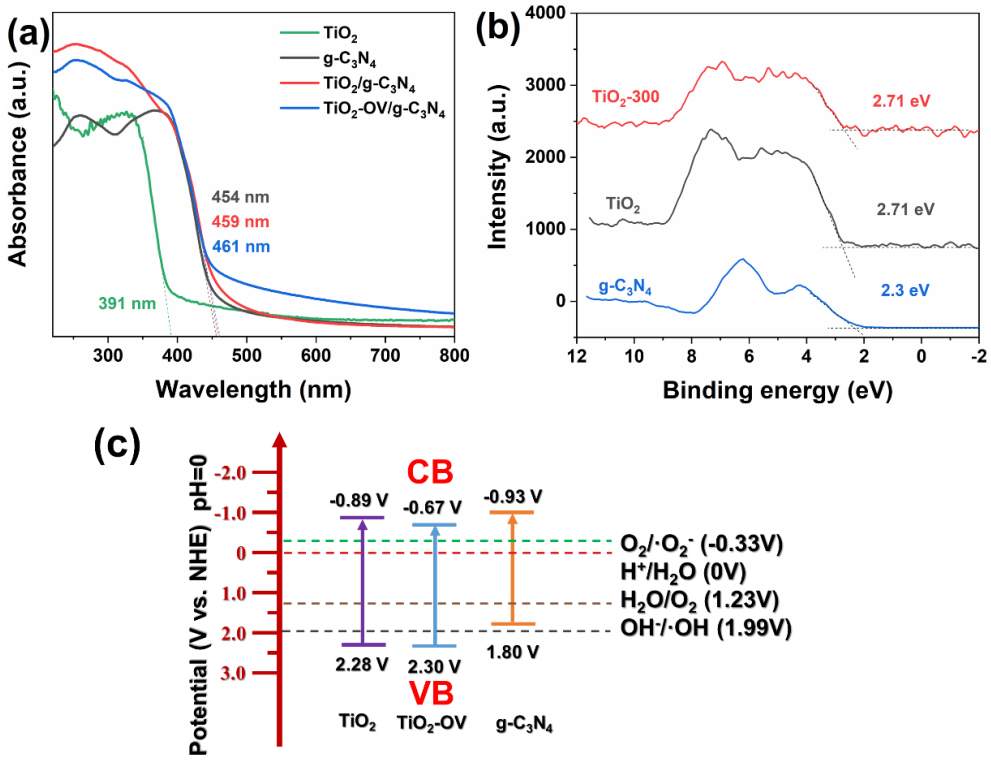

Figure 3. (a) UV-Vis DRS spectra of g-C_3N_4 NSs, TiO_2/g-C_3N_4, and TiO_2-OV/g-C_3N_4. (b) VB-XPS spectra and (c) band structures of TiO_2, TiO_2-OV and g-C_3N_4.

To probe the transfer direction of photoinduced electrons between TiO_2 QDs, TiO_2-OV and g-C_3N_4, their contact potential differences (CPD) were measured using KPFM [37]. As displayed in **Figure S10** and **Table S4**, the work functions of TiO_2 QDs, TiO_2-OV and g-C_3N_4 were calculated at 4.91, 4.77, and 4.56 eV, respectively. This means the electrons will migrate from g-C_3N_4 to TiO_2 QDs and TiO_2-OV upon contact without illumination.

The *in situ* irradiated XPS was further conducted to investigate the surface chemical states and photoinduced electrons migration over the photocatalysts. As displayed in **Figure 4a**, the peaks at 284.8 and 287.9 eV in the C 1s XPS spectra are related to surface adventitious carbon species (C–C/C=C) and sp^2-hybridized carbon in N=C–N aromatic rings, respectively [10, 38, 39]. These peaks in the TiO_2-OV/g-C_3N_4 heterojunction shifted toward higher binding energy (BE, ca. 288.2 eV) in darkness and lower BE (ca. 288 eV) under illumination, suggesting that the g-C_3N_4 was an electron donor without illumination, consistent with the CPD analyses, but an electron acceptor under light irradiation. The N 1s XPS spectra show a similar electron migration phenomenon. As displayed in **Figure 4b**, the typical peaks of N1s at 400.9, 399.7 and 398.5 eV correspond to surface amino N groups (N–H), three-coordinate N species ($N–(C)_3$), and sp^2-hybridized N atoms (C=N–C) in the triazine rings, respectively [10, 38, 39]. The BEs of the latter two N species shifted to higher range ($N–(C)_3$: 399.9 eV; C=N–C: 398.6 eV) in darkness but lower range ($N–(C)_3$: 399.4 eV; C=N–C: 398.4 eV) after light irradiation.

Additionally, to verify the electronic function of TiO_2-OV in the heterojunction, Ti 2p and O 1s XPS were measured. Two Ti 2p peaks at 458.9 and 464.6 eV (**Figure 4c**) can be observed corresponding to Ti $2p_{3/2}$ and Ti $2p_{1/2}$, respectively. Compared with TiO_2-OV, the BEs of Ti 2p (Ti $2p_{3/2}$: 458.5 eV; Ti $2p_{1/2}$: 464.3 eV) in TiO_2-OV/g-C_3N_4 composite obviously shifted to lower range in darkness, indicative of the TiO_2-OV as an electron acceptor without illumination. While under

illumination, the BEs of Ti 2p (Ti $2p_{3/2}$: 458.6 eV; Ti $2p_{1/2}$: 464.4 eV) shifted to a higher range, suggesting the role of electron donor. Similarity, the O 1s XPS spectra exhibit two peaks at approximately 530.2 and 531.4 eV (**Figure 4d**), corresponding to lattice oxygen (Ti–O) and surface-absorbed oxygen, respectively [38, 40]. The BE of lattice oxygen shifted to lower range (529.7 eV) in darkness and higher range (529.9 eV) after illumination [10, 38, 39]. The XPS results indicate that in darkness, the photoexcited carriers migrate from g-C_3N_4 to TiO_2-OV, while the photoelectrons migrate from the TiO_2-OV to g-C_3N_4 (opposite direction) under illumination, resulting in the S-scheme charge transfer pathway across the 0D/2D heterojunction.

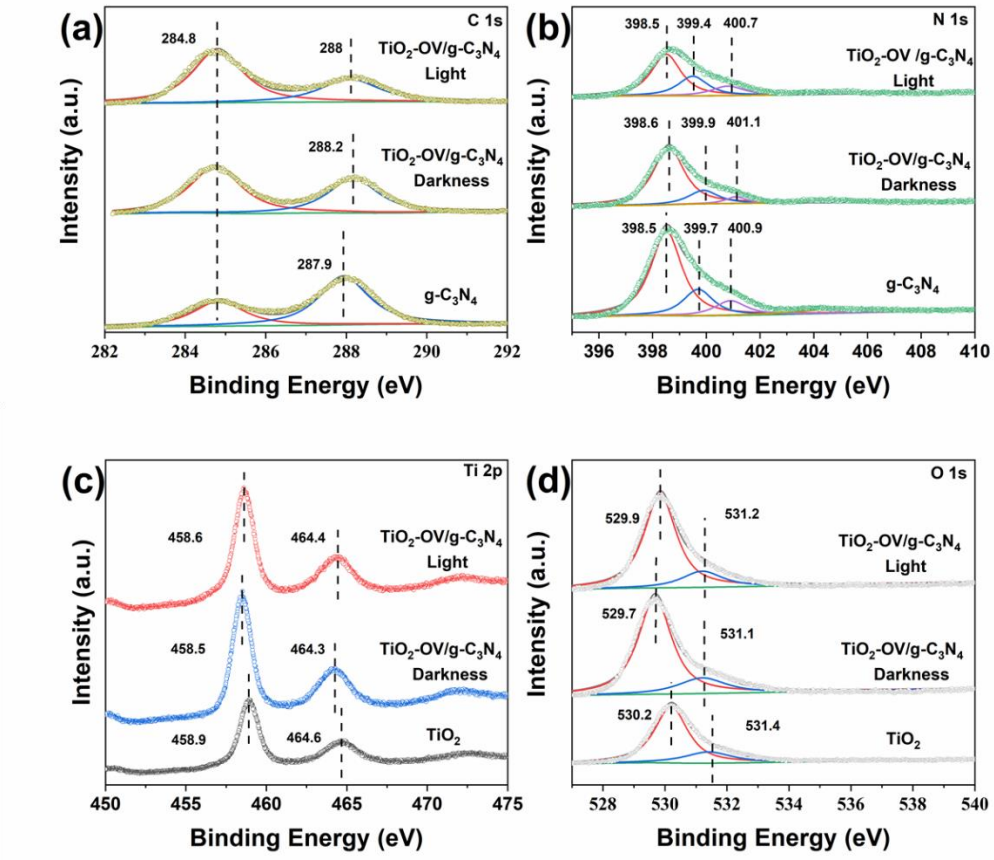

Figure 4. High-resolution XPS spectra of (a) C 1s (b) N 1s (c) Ti 2p (d) O 1s for g-C_3N_4, TiO_2 and TiO_2-OV/g-C_3N_4 samples tested in darkness and under 365 nm LED illumination.

EPR was further performed to demonstrate such an S-scheme pathway in the heterojunction under visible illumination. During the measurements, 5,5-dimethyl-1-pyrroline N-oxide (DMPO) was utilized to capture superoxide radicals ($\cdot O_2^-$) and hydroxyl radicals (·OH) [41]. As displayed in **Figure 5a and b**, under illumination, the TiO_2 QDs did not yield DMPO-$\cdot O_2^-$ and DMPO-·OH signals unsurprisingly, while for the TiO_2-OV, typical peaks of$\cdot O_2^-$ and·OH appeared, in good accordance with the UV-Vis DRS analyses (**Figure 3a**). For the g-C_3N_4, DMPO-$\cdot O_2^-$ EPR signal was observed, but DMPO-·OH EPR signal was not detected. because the reason is that the CB position (−0.93 V *vs.* NHE, pH=0) of g-C_3N_4 was more negative than the potential of $O_2/\cdot O_2^-$ (−0.33 V *vs.* NHE, pH=0), and its VB position (1.80 V *vs.* NHE, pH=0) was less positive than the potential of $OH^-/\cdot OH$ (1.99 V *vs.* NHE, pH=0) [11, 42]. Notably, after combining the TiO_2-OV and g-C_3N_4, both$\cdot O_2^-$ and·OH EPR signals were remarkably increased. This reveals that the 0D/2D heterojunction has a strong redox capability with a separated distribution of reduction sites (g-C_3N_4) and oxidation sites (TiO_2-OV), and forms the S-scheme structure (**Figure 5c,d**).

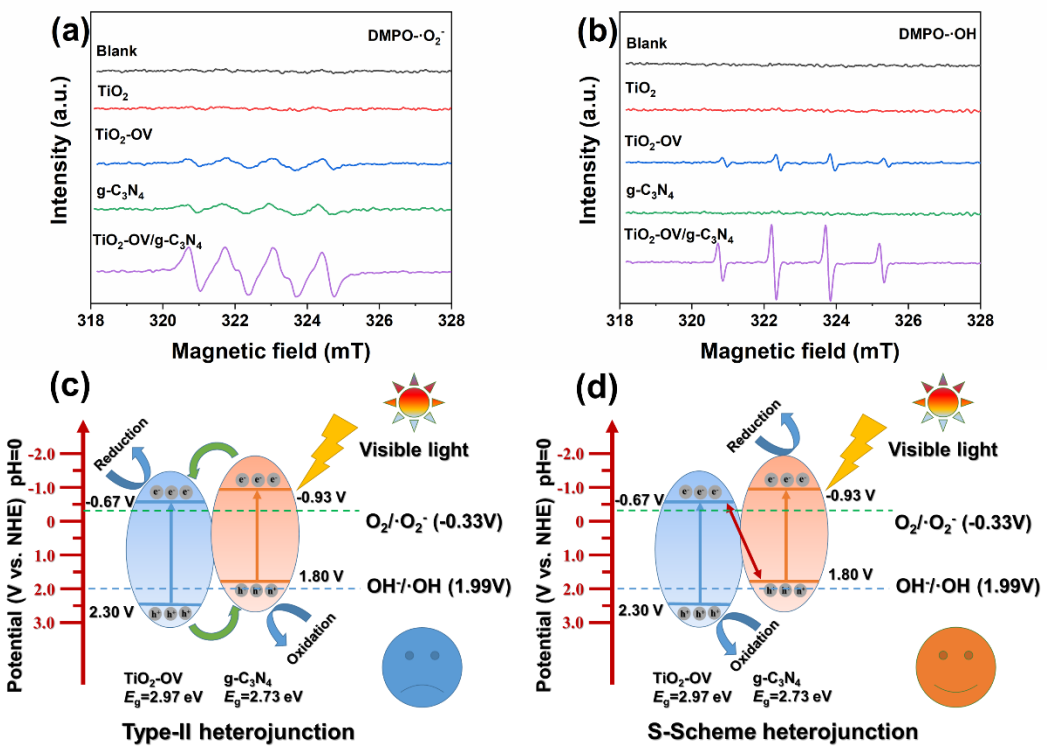

Figure 5. EPR signals of (a) DMPO-·O_2^- in methanol dispersions and (b) DMPO-·OH in aqueous dispersions over various photocatalysts under visible light irradiation for 300 s. The schematic illustration of photogenerated charge carrier transfer in (c) type-II heterojunction and (d) S-scheme heterojunction.

3.4 Photocatalytic activity measurements

To identify the benefits of vacancy-defect QDs and the S-scheme nature in the 0D/2D composite, visible-light photocatalytic HER performances of catalysts were then investigated with TEOA as hole-scavenge. The HER value of pure g-C_3N_4 (**Figure 6a**) was measured at approximately 104 μmol g^{-1} h^{-1}, which is similar to that reported earlier [43]. With loading TiO_2 particles at different sizes, the HER rates gradually increased with reducing the TiO_2 size. The highest HER rate was obtained by loading the TiO_2 QDs at ca. 30 wt% (**Figure S11**), which yielded a value of approximately 337 μmol g^{-1} h^{-1}. Such an improvement with reducing TiO_2 particle size has been attributed to gradually accelerated charge transfer and separation in TiO_2-to-bulk hybrids [5]. As confirmed by our DFT calculation, reducing the TiO_2 size from $Ti_{24}O_{48}$ to Ti_8O_{14}

298 significantly increased the electron density at the 0D/2D interfaces (**Figure 6c**), and reduce the
299 work function difference between TiO_2 and g-C_3N_4 (**Figure S12**). The accumulation of net charges
300 between the Ti_8O_{14}/g-C_3N_4 interfaces induced a strong internal electric field, greatly enhancing the
301 charge separation and transfer in the 0D/2D heterojunction. Furthermore, the planar-average
302 charge density difference along the Z direction (**Figure 6d**) proposes that electrons between the
303 Ti_8O_{14}/g-C_3N_4 interfaces mainly migrated from g-C_3N_4 to TiO_2 QDs without illumination,
304 consistent with the CPD and XPS results (**Figure 4** and **Figure S10**).

305 Following the preparation of TiO_2-OV/g-C_3N_4 heterojunction that were heat-treated as a final
306 step at temperatures in the range 100–300 °C, all samples exhibited improved HER performances
307 compared with pure g-C_3N_4 (**Figure S13**). The 100 and 200 °C aged samples exhibited relatively
308 similar HER rates to TiO_2 QDs/g-C_3N_4 heterojunction, because of their TiO_2-OV inactivation
309 under visible illumination (**Figure S8**), while the 300 °C-aged sample with an adsorption edge at
310 461 nm (see **Figure 3a**) has yielded a HER rate of approximately 1096 μmol g^{-1} h^{-1}, nearly 10-fold
311 higher than g-C_3N_4. Notably, such an improvement is universal for a great variety of carbon
312 nitrides, as by using the P-and O-modified g-C_3N_4 as a 2D host, the HER rate of the 0D/2D
313 heterojunction can be further increased to approximately 6308 μmol g^{-1} h^{-1} (see **Figure 6b**),
314 competing with the best reported carbon nitride photocatalysts to date (**Table S5**) [32, 44, 45].

315 In addition, the 0D/2D S-scheme heterojunction also showed a high oxidation ability in
316 photocatalytic degradation of rhodamine B. As displayed in **Figure S14** and **Table S6**, after
317 irradiation for 60 minutes, nearly 100% rhodamine B (k_a=0.0603) has been degraded over the
318 TiO_2-OV/g-C_3N_4 heterojunction. Its reaction rate is approximately 7 times that of the pristine g-
319 C_3N_4 (63%, k_a=0.0085). The stability of TiO_2-OV/g-C_3N_4 heterojunction was also estimated by
320 performing six reaction cycles with intermittent evacuation and re-loading of TEOA to compensate

for any losses after each run. As displayed in **Figure 6e** and supplementary **Figure S15−S17**, the cumulative H_2 evolution did not show obvious decrease in repeated runs, and the XRD, XPS, and FT-IR measurements on its textual properties did not show noticeable change after photocatalytic reaction, revealing a high photocatalytic stability of TiO_2-OV/g-C_3N_4 heterojunction.

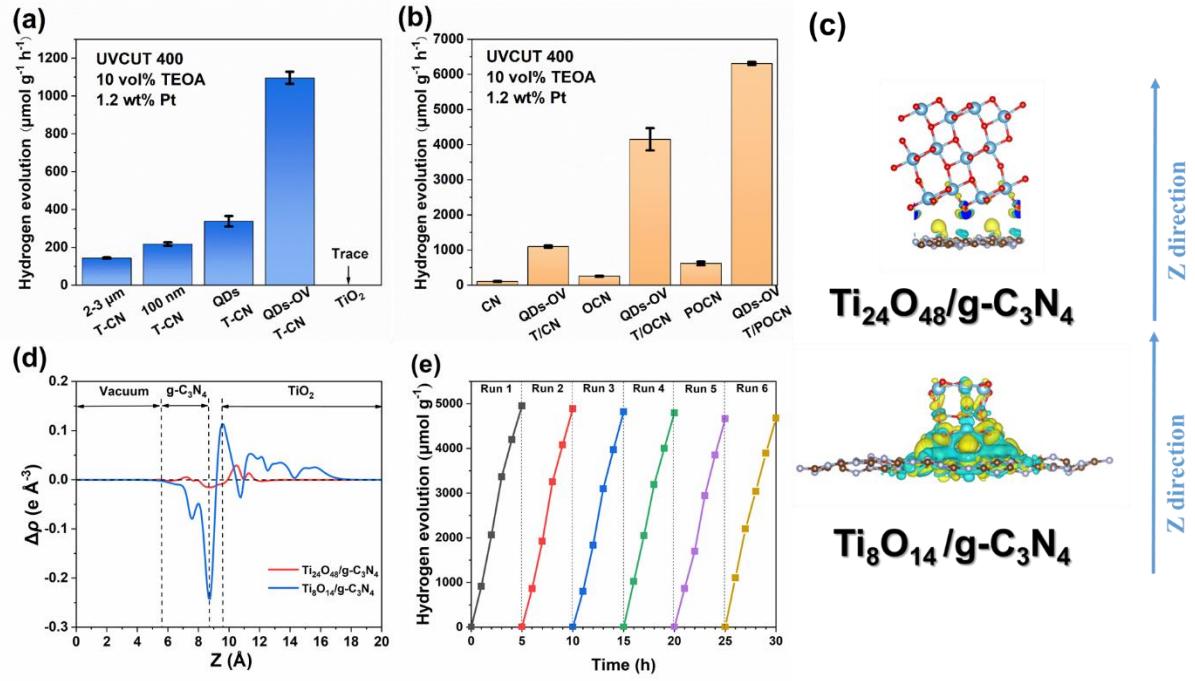

Figure 6. (a–b) Photocatalytic activities of different photocatalysts for H_2 evolution under visible light illumination (λ≥400 nm, 10 vol% TEOA as scavenger and 1.2 wt% H_2PtCl_6 as co-catalyst). (c) Charge density difference and (d) planar-averaged charge density difference along the Z direction of $Ti_{24}O_{48}$/g-C_3N_4 NSs and Ti_8O_{14}/g-C_3N_4 NSs (Charge accumulation is shown in yellow and charge depletion is labeled in blue, with an isovalue of 0.001 e Å^{-3}. Brown, light blue, blue and red spheres represent C, N, Ti, O atoms, respectively). (e) Cycling runs for photocatalytic activities on the TiO_2-OV/g-C_3N_4 heterojunction (aged at 300 °C).

Transfer kinetics of photoelectrons in the as-prepared samples were also investigated by using PL, TRPL, and electrochemical measurements. The PL spectra (see **Figure S18**) revealed both the TiO_2/g-C_3N_4 and TiO_2-OV/g-C_3N_4 displayed largely weakened emission signals compared with g-C_3N_4, which is owing to their considerably inhibited recombination rate and increased separation rate of photogenerated electrons at interfaces [46]. The TRPL decay spectra (see **Figure S19**)

estimated based on a double-exponential decay [47] shows that the intensity-average lifetimes ($<\tau>$) of emission decay was calculated at 4.45, 3.12, and 2.82 ns for g-C_3N_4, TiO_2/g-C_3N_4 and TiO_2-OV/g-C_3N_4, respectively (see **Table S7** and **Section S6**). The shortest lifetime in the TiO_2-OV/g-C_3N_4 heterojunction implies that defect engineering further enhances charge transfer at the 0D/2D interfaces [48]. The charge separation and recombination were determined by electrochemical impedance spectroscopy (EIS) characterization, which were presented in the form of Nyquist plots. The Nyquist plots in the EIS are displayed in **Figure S20**, where a smaller diameter suggests a faster rate of electron–hole separation and smaller charge transfer resistance [48]. TiO_2-OV/g-C_3N_4 had the smallest arc radius among all samples, indicating that it had the smallest charge transfer resistance and the defect engineering has also enhanced the photogenerated charge separation.

3.5 Reaction mechanism analyses

After identifying the function of vacancy-defect TiO_2 QDs for inducing S-scheme mechanism in the 0D/2D heterojunction, further investigations were performed to evaluate its reaction mechanism in photocatalytic H_2 evolution. In general, under an alkaline environment, the photocatalytic H_2 generation from water generally follows a four-step process when the TEOA is used as the sacrificial agent [10].

Step 1: $H_2O + * \rightarrow H_2O*$

Step 2: $H_2O* + * \rightarrow H* + OH*$ (Volmer step)

Step 3: $OH* + e^- \rightarrow OH^- + *$

$H* + H_2O* \rightarrow H_2* + OH*$ (Heyrovsky step)

$H* + H* \rightarrow H_2*$ (Tafel step)

Step 4: $H_2* \rightarrow H_2\ (g) + *$

where the adsorption and dissociation of H_2O molecules into H and OH groups on the semiconductor surface is an initial step (Volmer step), followed by the reaction between dissociated H* protons (Tafel step) or those with adsorbed H_2O* (Heyrovsky step) to form H_2*. The Volmer step is believed to be a rate-determining step, as either the Heyrovsky or Tafel step will be considerably accelerated over the Pt co-catalyst. This was verified by the fact that removing H_2PtCl_6 caused both the TiO_2/g-C_3N_4 and TiO_2-OV/g-C_3N_4, heterojunctions exhibiting poor HER performance under visible-light irradiation. Accordingly, our DFT calculations only considered the energetic favorability of the Volmer step in photocatalytic water splitting.

A model of platinum cluster (Pt_4) supported on the TiO_2/g-C_3N_4 system was constructed according to previous reports [49]. By comparing the adsorption energies of the Pt_4 cluster at different locations on TiO_2/g-C_3N_4 (namely Ti_8O_{14}/g-C_3N_4) and TiO_2-OV/g-C_3N_4 (namely Ti_8O_{13}/g-C_3N_4) heterojunctions (**Figure S21** and **Table S8-S9**), it was noted that the Pt_4 clusters tended to attach at the interface in both structures, which yielded the adsorption energies of −6.28 eV and −6.32 eV, respectively. Given the accumulation of photogenerated net charges at the interface of 0D/2D heterojunction (see **Figure 6c**), locating the Pt co-catalyst nearby the interface is expected to greatly facilitate the photochemical reaction (see **Figure 6a,b**).

In the Volmer reaction, H_2O was shown to preferentially adsorb near the Pt_4 cluster on Ti_8O_{14}/g-C_3N_4 heterojunction, with an adsorption energy of −0.91 eV (**Figure 7a**). The adsorbed H_2O is then dissociated into OH* and H*, with OH bound to the Pt site and H migrating to the neighboring O site. This step is exothermic by 0.81 eV, with an energy barrier of 0.10 eV. The Bader charge calculation (see **Figure 7b**) shows only 0.14 e charge transfer from the Ti_8O_{14}/g-C_3N_4 to adsorbed H_2O. In comparison, the Ti_8O_{13}/g-C_3N_4 heterojunction exhibits an H_2O adsorption energy of 1.62 eV, which is considerably higher than that of the Ti_8O_{14}/g-C_3N_4

heterojunction, suggesting that defect engineering can further enhance the H_2O adsorption on the 0D/2D heterojunction. Notably, the adsorbed H_2O on the Ti_8O_{13}/g-C_3N_4 heterojunction spontaneously dissociates into OH* without energy barrier, and compared with Ti_8O_{14}/g-C_3N_4 heterojunction, the Bader charge calculation shows a much higher charge transfer (0.34 e) on Ti_8O_{13}/g-C_3N_4 heterojunction. The DFT calculations indicate defect engineering effectively enhances the H_2O adsorption and dissociation on Pt/Ti_8O_{13}/g-C_3N_4 surface, and the Volmer reaction is more favorable on Ti_8O_{13}/g-C_3N_4 heterojunction than Ti_8O_{14}/g-C_3N_4. Furthermore, FT-IR (**Figure 7c**) and EPR analyses (**Figure 7d**) confirmed that the TiO_2-OV/g-C_3N_4 heterojunction yielded more intense vibration at approximately 3500 cm^{-1} (surface hydroxyl groups) [50, 51] after introducing saturated H_2O, and exhibited increased EPR signal for DMPO-·OH after irradiation, both of which are in agreement with the DFT calculations.

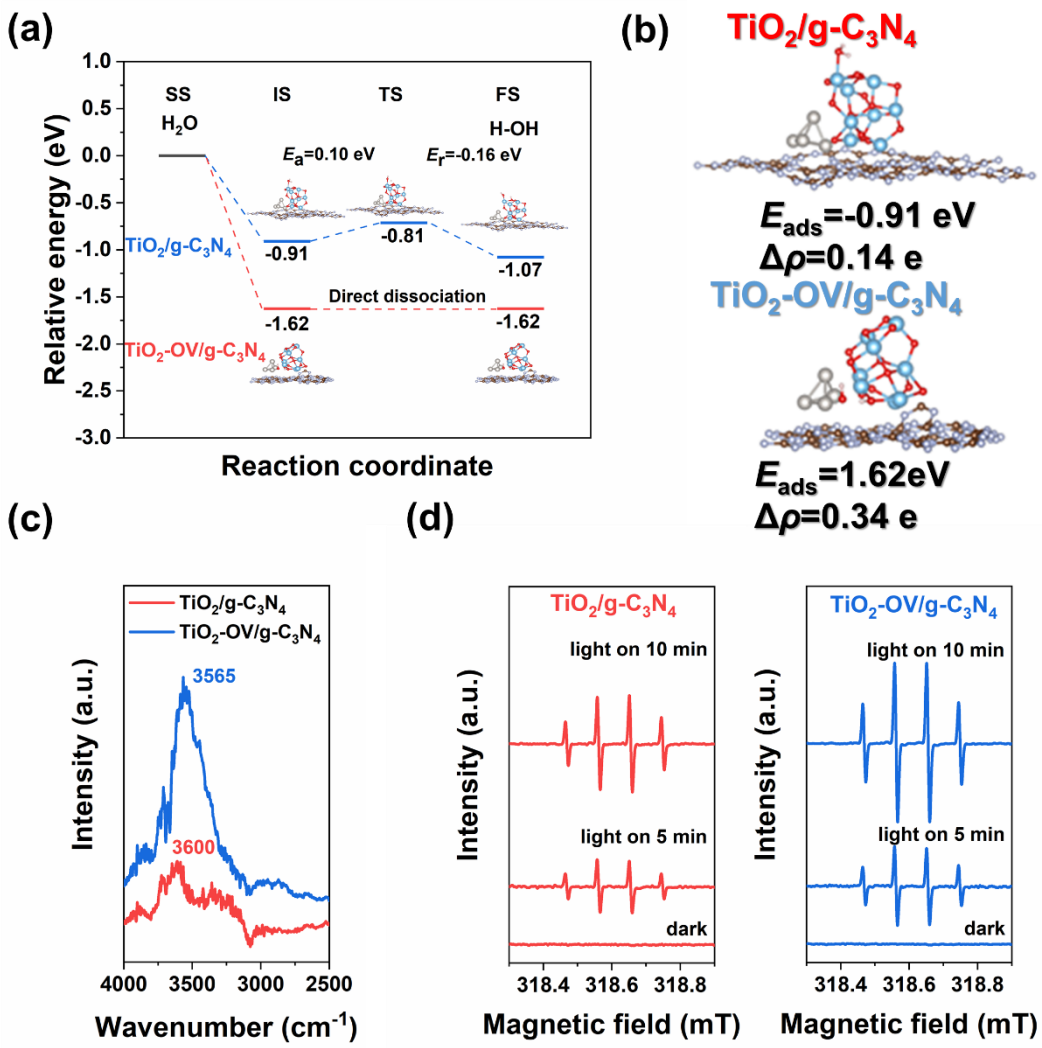

Figure 7. (a) Adsorption and reaction pathway of H_2O molecules on the TiO_2/g-C_3N_4 and TiO_2-OV/g-C_3N_4 (heat-treated at 300 °C) surface. "SS", "IS", "TS" and "FS"stand for the separate state, the initial state, the transition state, and the final state, respectively. The reference energy is that of the separate states. (b)Optimized geometric structure of H_2O molecules adsorption on TiO_2/g-C_3N_4 and TiO_2-OV/g-C_3N_4. E_{ads} is the adsorption energy of H_2O molecules. $\Delta\rho$ is the Bader charge change of the adsorbed H_2O, and positive values refer to the transportation of charge carriers from the catalyst surface to the adsorbed H_2O. (c) H_2O FT-IR spectra. (d) EPR spectra of the DMPO-·OH radicals.

4. Conclusions

An innovative vacancy-defect 0D/2D S-scheme heterojunction was successfully designed and constructed using a multistep assembly strategy. As part of this process, a highly scalable

continuous supercritical water flow reactor was employed for the synthesis of semiconductor QDs. Importantly, this synthetic route yielded TiO_2 QDs with abundant surface oxygen vacancies without changing the QD size. KPFM, in situ irradiated XPS, EPR measurements, and theoretical calculations provided strong evidence to confirm the S-scheme migration in the TiO_2-OV/g-C_3N_4 heterojunction, and indicated that the vacancy-defect 0D/2D S-scheme heterojunction has strong redox ability, superior interfacial charge separation and transfer efficiency, and barrierless H_2O dissociation ability, which essentially improves the photocatalytic hydrogen evolution under visible illumination. This study provides a perspective for manufacturing and optimizing vacancy-defect 0D/2D S-scheme heterojunctions. Mapping to the future, given the scalability for the QD continuous hydrothermal synthesis process (including a pilot scale facility in the lab of one of the co-authors and the potentiality of 1000 Ton nanoparticles (NPs) per year by the Hanwha Corporation facility [22]), it should be possible to perform large-scale production of defective semiconductor QDs and the corresponding 0D/2D composites. This will form part of our future endeavors which will be reported in due course.

Supporting Information.

Experimental section, schematic diagram, TEM, XRD Rietveld refinement, FT-IR, XPS, UV-Vis DRS, MS plots, CPDs, PALS, PL, TRPL, EIS, band structure, DFT calculations and additional figures for experimental and calculated results.

Notes

The authors declare no conflict of interest.

Acknowledgements

This work was supported by the National Natural Science Foundation of China (Grant No. 21922607, 51878598), the Outstanding Youth Project of Zhejiang Natural Science Foundation (Grant No. LR19E080004) and Key special project of "science and technology helps economy 2020" (Grant No. 2020ZLHJ01-4). The authors also wanted to acknowledge Prof. Jiaguo Yu (Wuhan University of Technology) for the help on in situ irradiated XPS measurements, Shiyanjia Lab (www.shiyanjia.com) for the support of KPFM tests and Perfectlight for the assistance of photocatalytic performance tests. JAD was supported by the JUICED energy hub (EPSRC reference EP/R023662/1).

References

[1] X.-B. Li, C.-H. Tung, L.-Z. Wu, Semiconducting quantum dots for artificial photosynthesis, Nat. Rev. Chem., 2 (2018) 160-173.

[2] S. Kundu, A. Patra, Nanoscale Strategies for Light Harvesting, Chem. Rev., 117 (2017) 712-757.

[3] G.H. Carey, A.L. Abdelhady, Z. Ning, S.M. Thon, O.M. Bakr, E.H. Sargent, Colloidal Quantum Dot Solar Cells, Chem. Rev., 115 (2015) 12732-12763.

[4] R.S. Selinsky, Q. Ding, M.S. Faber, J.C. Wright, S. Jin, Quantum dot nanoscale heterostructures for solar energy conversion, Chem. Soc. Rev., 42 (2013) 2963-2985.

[5] M.Y. Ye, Z.H. Zhao, Z.F. Hu, L.Q. Liu, H.M. Ji, Z.R. Shen, T.Y. Ma, 0D/2D Heterojunctions of Vanadate Quantum Dots/Graphitic Carbon Nitride Nanosheets for Enhanced Visible-Light-Driven Photocatalysis, Angew. Chem. Int. Ed., 56 (2017) 8407-8411.

[6] D.L. Huang, Z.H. Li, G.M. Zeng, C.Y. Zhou, W.J. Xue, X.M. Gong, X.L. Yan, S. Chen, W.J. Wang, M. Cheng, Megamerger in photocatalytic field: 2D g-C_3N_4 nanosheets serve as support of

448 0D nanomaterials for improving photocatalytic performance, Appl. Catal. B-Environ., 240 (2019)
449 153-173.
450 [7] J. Yang, H. Miao, J. Jing, Y. Zhu, W. Choi, Photocatalytic activity enhancement of PDI
451 supermolecular via π-π action and energy level adjusting with graphene quantum dots, Appl. Catal.
452 B-Environ., 281 (2021) 119547.
453 [8] J. Li, X. Wu, W. Pan, G. Zhang, H. Chen, Vacancy-Rich Monolayer BiO_{2-x} as a Highly
454 Efficient UV, Visible, and Near-Infrared Responsive Photocatalyst, Angew. Chem. Int. Ed., 57
455 (2018) 491-495.
456 [9] Z. Chen, Y. Deng, L. Tang, C. Feng, J. Wang, J. Yu, J. Wang, Z. Liu, H. Zhou, Theoretical
457 and experimental study of full spectrum response Z-scheme 0D/2D $Ag_6Si_2O_7$/CN photocatalyst
458 with enhanced photocatalytic activities, Appl. Surf. Sci., 514 (2020) 145963.
459 [10] J. Fu, Q. Xu, J. Low, C. Jiang, J. Yu, Ultrathin 2D/2D WO_3/g-C_3N_4 step-scheme H_2-
460 production photocatalyst, Appl. Catal. B-Environ., 243 (2019) 556-565.
461 [11] Q. Xu, L. Zhang, B. Cheng, J. Fan, J. Yu, S-Scheme Heterojunction Photocatalyst, Chem, 6
462 (2020) 1543-1559.
463 [12] S. Wageh, A.A. Al-Ghamdi, R. Jafer, X. Li, P. Zhangc, A new heterojunction in
464 photocatalysis: S-scheme heterojunction, Chin. J. Catal., 42 (2021) 667-669.
465 [13] C. Cheng, B. He, J. Fan, B. Cheng, S. Cao, J. Yu, An Inorganic/Organic S-Scheme
466 Heterojunction H_2-Production Photocatalyst and its Charge Transfer Mechanism, Adv. Mater., 33
467 (2021) 2100317.
468 [14] Y. Chen, M. Xu, J. Wen, Y. Wan, Q. Zhao, X. Cao, Y. Ding, Z.L. Wang, H. Li, Z. Bian,
469 Selective recovery of precious metals through photocatalysis, Nat. Sustain., 4 (2021) 618-626.

[15] X.-Y. Liu, G. Zhang, H. Chen, H. Li, J. Jiang, Y.-T. Long, Z. Ning, Efficient defect-controlled photocatalytic hydrogen generation based on near-infrared Cu-In-Zn-S quantum dots, Nano Res., 11 (2018) 1379-1388.

[16] F. Kayaci, S. Vempati, I. Donmez, N. Biyikli, T. Uyar, Role of zinc interstitials and oxygen vacancies of ZnO in photocatalysis: a bottom-up approach to control defect density, Nanoscale, 6 (2014) 10224-10234.

[17] J. Wang, L. Yu, Z. Wang, W. Wei, K. Wang, X. Wei, Constructing 0D/2D Z-Scheme Heterojunction of CdS/g-C_3N_4 with Enhanced Photocatalytic Activity for H_2 Evolution, Catal. Lett., 151 (2021) 3550-3561.

[18] M. Ou, W. Tu, S. Yin, W. Xing, S. Wu, H. Wang, S. Wan, Q. Zhong, R. Xu, Amino-Assisted Anchoring of $CsPbBr_3$ Perovskite Quantum Dots on Porous g-C_3N_4 for Enhanced Photocatalytic CO_2 Reduction, Angew. Chem. Int. Ed., 57 (2018) 13570-13574.

[19] L. Wang, Y. Wang, T. Xu, H. Liao, C. Yao, Y. Liu, Z. Li, Z. Chen, D. Pan, L. Sun, M. Wu, Gram-scale synthesis of single-crystalline graphene quantum dots with superior optical properties, Nat. Commun., 5 (2014) 5357.

[20] K.T. Yong, W.C. Law, R. Hu, L. Ye, L. Liu, M.T. Swihart, P.N. Prasad, Nanotoxicity assessment of quantum dots: from cellular to primate studies, Chem. Soc. Rev., 42 (2013) 1236-1250.

[21] J.A. Darr, J. Zhang, N.M. Makwana, X. Weng, Continuous Hydrothermal Synthesis of Inorganic Nanoparticles: Applications and Future Directions, Chem. Rev., 117 (2017) 11125-11238.

[22] T. Adschiri, Y.-W. Lee, M. Goto, S. Takami, Green materials synthesis with supercritical water, Green Chem., 13 (2011) 1380–1390.

493 [23] X. Weng, Q. Zeng, Y. Zhang, F. Dong, Z. Wu, Facile Approach for the Syntheses of Ultrafine
494 TiO_2 Nanocrystallites with Defects and C Heterojunction for Photocatalytic Water Splitting, ACS
495 Sustain. Chem. Eng., 4 (2016) 4314-4320.
496 [24] X. Weng, Y. Zhang, F. Bi, F. Dong, Z. Wu, J.A. Darr, Thermocatalytic syntheses of highly
497 defective hybrid nano-catalysts for photocatalytic hydrogen evolution, J. Mater. Chem. A, 5 (2017)
498 23766-23775.
499 [25] P. Niu, L. Zhang, G. Liu, H.-M. Cheng, Graphene-Like Carbon Nitride Nanosheets for
500 Improved Photocatalytic Activities, Adv. Funct. Mater., 22 (2012) 4763-4770.
501 [26] X. Zhang, X. Xie, H. Wang, J. Zhang, B. Pan, Y. Xie, Enhanced Photoresponsive Ultrathin
502 Graphitic-Phase C_3N_4 Nanosheets for Bioimaging, J. Am. Chem. Soc., 135 (2013) 18-21.
503 [27] G. Kresse, J. Furthmuller, Efficient iterative schemes for ab initio total-energy calculations
504 using a plane-wave basis set, Phys. Rev. B, 54 (1996) 11169-11186.
505 [28] H. Li, J. Shang, Z. Ai, L. Zhang, Efficient Visible Light Nitrogen Fixation with BiOBr
506 Nanosheets of Oxygen Vacancies on the Exposed {001} Facets, J. Am. Chem. Soc., 137 (2015)
507 6393-6399.
508 [29] M. Guan, C. Xiao, J. Zhang, S. Fan, R. An, Q. Cheng, J. Xie, M. Zhou, B. Ye, Y. Xie, Vacancy
509 Associates Promoting Solar-Driven Photocatalytic Activity of Ultrathin Bismuth Oxychloride
510 Nanosheets, J. Am. Chem. Soc., 135 (2013) 10411-10417.
511 [30] X. Jiang, Y. Zhang, J. Jiang, Y. Rong, Y. Wang, Y. Wu, C. Pan, Characterization of Oxygen
512 Vacancy Associates within Hydrogenated TiO_2: A Positron Annihilation Study, J. Phys. Chem. C,
513 116 (2012) 22619-22624.

[31] Z. Huang, Q. Sun, K. Lv, Z. Zhang, M. Li, B. Li, Effect of contact interface between TiO_2 and g-C_3N_4 on the photoreactivity of g-C_3N_4/TiO_2 photocatalyst: (001) vs (101) facets of TiO_2, Appl. Catal. B-Environ., 164 (2015) 420-427.

[32] X. Wang, K. Maeda, A. Thomas, K. Takanabe, G. Xin, J.M. Carlsson, K. Domen, M. Antonietti, A metal-free polymeric photocatalyst for hydrogen production from water under visible light, Nat. Mater., 8 (2009) 76-80.

[33] L. Kavan, M. Grätzel, S.E. Gilbert, C. Klemenz, H.J. Scheel, Electrochemical and Photoelectrochemical Investigation of Single-Crystal Anatase, J. Am. Chem. Soc., 118 (1996) 6716-6723.

[34] L.K. Putri, B.-J. Ng, W.-J. Ong, H.W. Lee, W.S. Chang, S.-P. Chai, Engineering nanoscale p–n junction via the synergetic dual-doping of p-type boron-doped graphene hybridized with n-type oxygen-doped carbon nitride for enhanced photocatalytic hydrogen evolution, J. Mater. Chem. A, 6 (2018) 3181-3194.

[35] Z. Hu, G. Liu, X. Chen, Z. Shen, J.C. Yu, Enhancing Charge Separation in Metallic Photocatalysts: A Case Study of the Conducting Molybdenum Dioxide, Adv. Funct. Mater., 26 (2016) 4445-4455.

[36] N. Tian, Y. Zhang, X. Li, K. Xiao, X. Du, F. Dong, G.I.N. Waterhouse, T. Zhang, H. Huang, Precursor-reforming protocol to 3D mesoporous g-C_3N_4 established by ultrathin self-doped nanosheets for superior hydrogen evolution, Nano Energy, 38 (2017) 72-81.

[37] Z. Xing, J. Hu, M. Ma, H. Lin, Y. An, Z. Liu, Y. Zhang, J. Li, S. Yang, From One to Two: In Situ Construction of an Ultrathin 2D-2D Closely Bonded Heterojunction from a Single-Phase Monolayer Nanosheet, J. Am. Chem. Soc., 141 (2019) 19715-19727.

[38] F. He, B. Zhu, B. Cheng, J. Yu, W. Ho, W. Macyk, 2D/2D/0D $TiO_2/C_3N_4/Ti_3C_2$ MXene composite S-scheme photocatalyst with enhanced CO_2 reduction activity, Appl. Catal. B-Environ., 272 (2020) 119006.

[39] P. Xia, S. Cao, B. Zhu, M. Liu, M. Shi, J. Yu, Y. Zhang, Designing a 0D/2D S-Scheme Heterojunction over Polymeric Carbon Nitride for Visible-Light Photocatalytic Inactivation of Bacteria, Angew. Chem. Int. Ed., 59 (2020) 5218-5225.

[40] L. Wang, B. Cheng, L. Zhang, J. Yu, In situ Irradiated XPS Investigation on S-Scheme $TiO_2@ZnIn_2S_4$ Photocatalyst for Efficient Photocatalytic CO_2 Reduction, Small, (2021) 2103447.

[41] S. Xu, P. Zhou, Z. Zhang, C. Yang, B. Zhang, K. Deng, S. Bottle, H. Zhu, Selective Oxidation of 5-Hydroxymethylfurfural to 2,5-Furandicarboxylic Acid Using O_2 and a Photocatalyst of Co-thioporphyrazine Bonded to g-C_3N_4, J. Am. Chem. Soc., 139 (2017) 14775-14782.

[42] C. Liu, D. Kong, P.C. Hsu, H. Yuan, H.W. Lee, Y. Liu, H. Wang, S. Wang, K. Yan, D. Lin, P.A. Maraccini, K.M. Parker, A.B. Boehm, Y. Cui, Rapid water disinfection using vertically aligned MoS_2 nanofilms and visible light, Nat. Nanotechnol., 11 (2016) 1098-1104.

[43] Q. Xiang, J. Yu, M. Jaroniec, Preparation and Enhanced Visible-Light Photocatalytic H_2-Production Activity of Graphene/C_3N_4 Composites, J. Phys. Chem. C, 115 (2011) 7355-7363.

[44] W.J. Ong, L.L. Tan, Y.H. Ng, S.T. Yong, S.P. Chai, Graphitic Carbon Nitride (g-C_3N_4)-Based Photocatalysts for Artificial Photosynthesis and Environmental Remediation: Are We a Step Closer To Achieving Sustainability?, Chem. Rev., 116 (2016) 7159-7329.

[45] X. Chen, R. Shi, Q. Chen, Z. Zhang, W. Jiang, Y. Zhu, T. Zhang, Three-dimensional porous g-C_3N_4 for highly efficient photocatalytic overall water splitting, Nano Energy, 59 (2019) 644-650.

[46] Z. Lu, L. Zeng, W. Song, Z. Qin, D. Zeng, C. Xie, In situ synthesis of C-TiO_2/g-C_3N_4 heterojunction nanocomposite as highly visible light active photocatalyst originated from effective interfacial charge transfer, Appl. Catal. B-Environ., 202 (2017) 489-499.

[47] M.Z. Ge, C.Y. Cao, S.H. Li, Y.X. Tang, L.N. Wang, N. Qi, J.Y. Huang, K.Q. Zhang, S.S. Al-Deyab, Y.K. Lai, In situ plasmonic Ag nanoparticle anchored TiO_2 nanotube arrays as visible-light-driven photocatalysts for enhanced water splitting, Nanoscale, 8 (2016) 5226-5234.

[48] M. Wang, D. Zheng, M. Ye, C. Zhang, B. Xu, C. Lin, L. Sun, Z. Lin, One-Dimensional Densely Aligned Perovskite-Decorated Semiconductor Heterojunctions with Enhanced Photocatalytic Activity, Small, 11 (2015) 1436-1442.

[49] F. Liu, P. Xiao, E. Uchaker, H. He, M. Zhou, X. Zhou, Y. Zhang, A first-principles study of Pt–Ni bimetallic cluster adsorption on the anatase TiO_2 (1 0 1) surface: Probing electron effect of Ni in TiO_2 (1 0 1)-bimetallic cluster (Pt–Ni) on the adsorption and dissociation of methanol, Appl. Surf. Sci., 315 (2014) 81-89.

[50] W. Hage, K.R. Liedl, A. Hallbrucker, E. Mayer, Carbonic Acid in the Gas Phase and Its Astrophysical Relevance, Science, 279 (1998) 1332-1335.

[51] N.Y. Topsoe, Mechanism of the Selective Catalytic Reduction of Nitric Oxide by Ammonia Elucidated by in Situ On-Line Fourier Transform Infrared Spectroscopy, Science, 265 (1994) 1217-1219.